Microgravity and Transfer/Solidification, crystal growth from the melt

Convection modeling in directional solidification

Juan C. Heinrich [a,*], David R. Poirier [b]

[a] *Department of Aerospace and Mechanical Engineering, The University of Arizona, Tucson, AZ 85721, USA*
[b] *Department of Materials Science and Engineering, The University of Arizona, Tucson, AZ 85721, USA*

Abstract

Mathematical and numerical models of solidification of binary and multicomponent dendritic alloys that can model the dynamics of the mushy zone as well as the all liquid region are examined. The discussion is centered around models based on finite element discretization of the governing equations that have been developed by the authors during the last fifteen years. The capabilities of existing simulation codes to model the effects of convection and the resulting macrosegregation in castings, and in particular, the development of 'freckles' in vertically solidified dendritic monocrystals are discussed. The current capabilities of the models as well as the areas in which more improvement is needed are noted. Numerical examples are presented to illustrate the different aspects of the simulations. *To cite this article: J.C. Heinrich, D.R. Poirier, C. R. Mecanique 332 (2004).*
© 2004 Académie des sciences. Published by Elsevier SAS. All rights reserved.

Résumé

Modélisation de la convection au cours de la solidification directionnelle. Nous exposons des modèles mathématiques et numériques de la solidification d'alliages dendritiques, binaires et multiconstituants, qui peuvent décrire la dynamique de la zone pâteuse ainsi que la région liquide. La discussion est centrée sur des modèles développés par les auteurs du présent article et basés sur la discrétisation en éléments finis des équations qui régissent les phénomènes. Nous discutons la capacité des programmes de simulation existants à modéliser les effets de la convection et de la macroségrégation qui en résulte dans les pièces coulées, et plus particulièrement la formation de « freckles » dans les monocristaux dendritiques solidifiés verticalement. Nous faisons ressortir les limites actuelles des modèles ainsi que les domaines dans lesquels des améliorations sont nécessaires. Des exemples numériques illustrent les différent aspects des simulations. *Pour citer cet article : J.C. Heinrich, D.R. Poirier, C. R. Mecanique 332 (2004).*
© 2004 Académie des sciences. Published by Elsevier SAS. All rights reserved.

Keywords: Dendritic solidification; Multicomponent alloys; Binary alloys; Directional solidification; Macrosegregation

Mots-clés : Solidification dendritiques ; Alliages multiconstituants ; Alliages binaires ; Solidification directionnelle ; Macroségrégation

---

* Corresponding author.
 E-mail addresses: juanh@u.arizona.edu (J.C. Heinrich), poirierd@u.arizona.edu (D.R. Poirier).

1. Introduction

Macrosegregation in castings remains a serious problem that producers of ingots and castings must deal with on a day-by-day basis. At the same time, an increasing number of technological applications require that critical mechanical components operate at extreme conditions of temperature and stress, underscoring the necessity and importance of sound computational models of solidification that can guide the design of the processes, with the aim of reducing scrap and the expense of evaluating full scale production runs in order to realize a method to successfully make the ingots or castings.

Although castings are susceptible to many types of defects, macrosegregation can be the major factor that limits the size of the cast-product. One of the most dramatic examples of macrosegregation defects is found in the directional solidification of single-crystal superalloy turbine blades, where the level of rejection at the end of the manufacturing process can reach around 40% [1,2]. Directional solidification provides the means to control the grain shape, producing columnar microstructures with the grain boundaries aligned parallel to the longitudinal direction of the casting. The process can be further improved by casting single crystals in which only one columnar grain is allowed to grow, thus greatly improving the creep resistance at elevated temperatures [3]. In this process solidification is effected vertically under a stable temperature gradient established by extracting heat at the bottom of the casting via a water-cooled 'chill' and by radiation to a cold zone.

Without proper control, macrosegregation defects can develop in directionally solidified castings; in particular, vertically solidified monocrystals are susceptible to developing 'freckles'. These are localized segregates in the form of long narrow trails aligned parallel to the direction of gravity, enriched in the normally segregating elements, depleted of the inversely segregating elements and with a width length of 1–2 mm.

Within the casting community there has been a large volume of research and modeling efforts over the past forty years. This has led to numerical models of solidification that can be categorized into three types according to the length scales that they resolve. (i) Macroscale models can be utilized for simulations of full castings with dimensions on the order of a meter. Typically they model the mold filling process and the heat transfer process, but, so far, cannot include detailed models of the mushy zone. Some codes are commercially available; a review of these codes is found in [4]. For filling, the models underlying the codes are based on the classical volume of fluid (VOF) approach; more recent algorithms based on moving Lagrangian interface techniques are discussed in [5]. (ii) Mesoscale models are capable of modeling solidification domains of length scales on the order of 1–10 centimeters and treat the mushy zone as an anisotropic porous medium, using either mixture theory or volume average formulations, and are the focus of this article. The main difficulty in applying these models at larger scales is their current lack of efficiency; these issues will be discussed in a later section. (iii) Microscale models that can follow the development of individual dendrites and, at this time, model length scales at the dendritic level in domains up to several millimeters. These models have been applied to simulations of dendritic and cellular solidification of pure substances in undercooled liquids [6–9], but less so for the binary alloys [10–12].

Early mesoscale models of dendritic solidification of alloys date back to the early 1960s, and their emphasis was on solute redistribution and macrosegregation [13–27]. Thermosolutal convection in the liquid was not considered, but it was recognized that the density of the interdendritic liquid varies spatially and temporally within the mushy zone, so buoyancy-driven convection of the interdendritic liquid was calculated. These analyses were sufficient to describe macrosegregation when thermosolutal convection in the all-liquid zone is not important and when the geometry of the mushy zone is prescribed, but cannot capture the formation of freckles or channel segregates, which involves partial remelting of the dendrites due to thermosolutal convection in the all-liquid zone and its interaction with the mushy zone. Numerical models that include thermosolutal convection in the mushy zone and the liquid appeared in the mid-1980s; these are usually referred to as one-domain models or continuum models, because the equations are developed using mixture theory or volume averaging [28–31] that precludes the need to model the interface between the all-liquid zone and the mushy zone. The latter is treated as a porous medium with variable anisotropic permeability; the fluid flow problem becomes that of analyzing the motion of a layer of fluid overlying a porous medium. It is governed by a single momentum equation that can be solved using finite

differences, finite volumes or finite elements, in a single domain discretized with a fixed computational mesh [32–40]. Reviews are presented in [41–43]. In this article the mathematical model is presented and discussed in the next section; the current capabilities and outstanding modeling issues are discussed in Section 3 in relation to the convection-modeling in both the terrestrial and microgravity environments; in Section 4 some illustrative examples are discussed.

2. Mathematical model of solidification

The continuum equations of continuity, momentum, conservation of energy and conservation of solute species have been developed using the volume averaging technique of [29,30]. For this article, we invoke the following assumptions:

(1) Flow of interdendritic liquid is laminar, incompressible and Newtonian;
(2) Two phases, liquid and solid, are considered; no pores form;
(3) The solid, once it forms, is stationary, and there is no solute-diffusion in the solid;
(4) The density of the solid may be different than the density of the liquid, but both are constant;
(5) Other properties of the liquid and solid, other than the specific heat capacity, are equal and constant in both phases;
(6) The mushy zone behaves as a porous medium with a variable and anisotropic permeability.

Assumptions (4) and (5) are not necessary in this model, but they greatly simplify the presentation. Simulations using variable properties were presented in [37].

The volumetric enthalpy, $\bar{\rho}\bar{h}$, is expressed as

$$\bar{\rho}\bar{h} = \rho_s h_s (1 - \phi) + \rho_\ell h_\ell \phi \tag{1}$$

Here, h_s and h_ℓ are the intensive enthalpies (J/kg) in the solid and liquid, respectively; ρ_s and ρ_ℓ are the densities (kg/m^3) of the solid and liquid; and ϕ is the volume fraction of liquid. It is assumed that, within the mushy zone, the enthalpies can be expressed as a linear function of temperature as

$$\begin{aligned} h_s &= c_{p_s} T \\ h_\ell &= c_{p_\ell} T + (c_{p_s} - c_{p_\ell}) T_H + L \end{aligned} \tag{2}$$

where L is the latent heat (J/kg) at the reference temperature T_H, T is temperature (K), and c_{p_s} and c_{p_ℓ} are the specific heat capacities (J/kg K) in the solid and liquid phases, respectively, which are assumed to be constants.

From Eq. (25b) in [29], the continuity equation becomes

$$\nabla \cdot \rho_\ell \mathbf{u} = \beta \frac{\partial \phi}{\partial t} \tag{3}$$

where $\beta = (\rho_s - \rho_\ell)/\rho_\ell$ is the contraction ratio (or solidification contraction) and $\mathbf{u}$ is the superficial velocity (m/s). The momentum equation is obtained from Eq. (43) in [29],

$$\frac{\partial \mathbf{u}}{\partial t} + \frac{\mathbf{u}}{\phi} \cdot \nabla \mathbf{u} - \frac{\beta}{\phi} \frac{\partial \phi}{\partial t} \mathbf{u} = -\frac{\phi}{\rho_\ell} \nabla p + \nu \left[\nabla^2 \mathbf{u} + \frac{\beta}{3} \nabla \frac{\partial \phi}{\partial t} \right] - \nu \phi \mathbf{K}^{-1} \mathbf{u} + \frac{\rho \phi}{\rho_\ell} \mathbf{g} \tag{4}$$

where ν is the kinematic viscosity (m^2/s), p is pressure (Pa), $\mathbf{K}$ is the permeability tensor (m^2), and $\mathbf{g}$ is the gravitational acceleration (m/s^2). Eq. (4) differs from the momentum equation obtained using mixture theory that was used in [28] in the form of the viscous term and the explicit influence of the volume fraction of liquid, ϕ.

The Boussinesq approximation is used to account for buoyancy effects in the liquid; that is the density ρ in the buoyancy term is assumed to obey a linear relation of the form

$$\rho = \rho_\ell \left[1 + \beta_T (T - T_0) + \sum_{j=0}^{N} \beta_C^j (C_\ell^j - C_0^j) \right] \tag{5}$$

In Eq. (5), C_ℓ^j is the solute concentration in the liquid of alloy component j; N is the number of alloy components; the subscript 0 denotes the reference temperature and concentration at which ρ_ℓ is given, and β_T and β_C^j are, respectively, the thermal and solutal coefficients of volumetric expansion.

In Eq. (4), the viscous term is known as the Brinkman term, and it allows us to have a continuous transition from the liquid layer to the porous medium representing the mushy zone [44]. A second-order friction term [45], or Forschheimer term, is omitted because in our experience, it does not appear to have any measurable effects in the numerical calculations. In the work of some authors, e.g., [36,46], the Forschheimer term has been retained.

The average density $\bar{\rho}$ and the average total concentration of mass for each solute species $\bar{\rho}\overline{C}^j$ are given, respectively, by

$$\bar{\rho} = \rho_s (1 - \phi) + \rho_\ell \phi \tag{6}$$

and

$$\bar{\rho}\overline{C} = \rho_s C_s^j (1 - \phi) + \rho_\ell C_\ell^j \phi \tag{7}$$

which is the form used by Flemings and Nereo [14]; C_s^j is the solute concentration of element j in the solid, for the case of no diffusion in the solid these are given by

$$C_s^j = \frac{1}{1 - \phi} \int_\phi^1 k_j C_\ell^j \, \mathrm{d}\phi \tag{8}$$

where k_j is the partition coefficient of element j.

The equations of conservation of solute are obtained from Eq. (18) in [30] and are

$$\frac{\partial \bar{\rho}\overline{C}^j}{\partial t} = -\rho_\ell \left[\beta C_\ell^j \frac{\partial \phi}{\partial t} + \mathbf{u} \cdot \nabla C_\ell^j - D\nabla \cdot \phi \nabla C_\ell^j \right] \tag{9}$$

The energy equation is written in terms of temperature only and is derived from Eq. (10) in [30] and Eqs. (1) and (2) above; it takes the form

$$\bar{\rho}\bar{c}_p \frac{\partial T}{\partial t} + \rho_s \left[(c_{p_s} - c_{p_\ell})(T_H - T) + L \right] \frac{\partial \phi}{\partial t} + \rho_\ell c_{p_\ell} \mathbf{u} \cdot \nabla T = \nabla \cdot \kappa \nabla T \tag{10}$$

where the mixture heat capacity, $\overline{\rho c}_p$, is

$$\overline{\rho c}_p = \rho_s c_{p_s} (1 - \phi) + \rho_\ell c_{p_\ell} \phi \tag{11}$$

and κ is the constant thermal conductivity (W/m K) of the mixture.

To complete the model it is assumed that no undercooling takes place in the mushy zone and that the liquidus temperature of the alloy is a function of its local composition, which we express in the form

$$T = F(C_\ell^j) \tag{12}$$

In the particular case of a binary alloy, it is assumed that the partition coefficient, k, is a constant and the liquidus line is straight. The liquidus temperature is then given by

$$T = mC_\ell + T_m \tag{13}$$
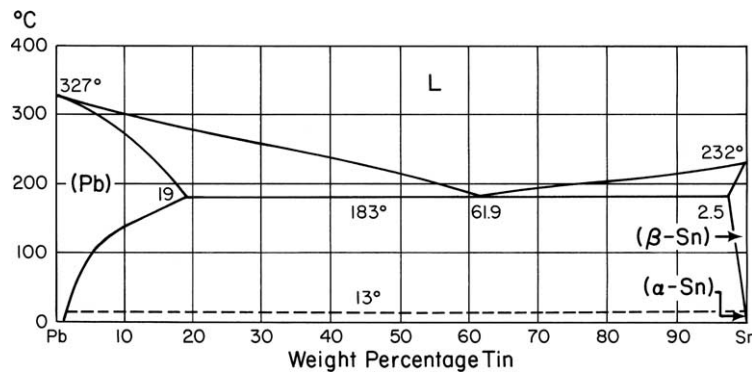
Fig. 1. Phase diagram for Pb–Sn alloys.

Fig. 1. Diagramme d'équilibre des phases pour le système Pb–Sn.

Fig. 1 shows the phase diagram for binary Pb–Sn alloys; clearly the liquidus line can be well approximated by a straight line. The assumption of a constant partition coefficient k is not as good due to the curvature of the solidus line close to the pure Pb side; however, it is still accurate enough for solutions that are not very dilute.

The non-dimensionalization of the equations has been addressed in several publications [33,47,48], and an analysis of the parameter ranges for the case of directional solidification from a side wall was presented in [49]. Although the exact form of the equations used by different authors varies, they all follow the same basic premises and assumptions so results are generally comparable. A difference is the choice of the permeability $\mathbf{K}$ in Eq. (4) that is discussed below.

3. Numerical models of solidification

Eqs. (3), (4), (9) and (10) (or their counterparts) have been discretized using finite differences [35], finite elements [33,39,40], and finite volume methods [32,36–38,40]. All the models use a fixed computational grid and determine the location of the mushy zone using the fraction of liquid as a dependent variable. The calculations presented in this article have been done using a finite element algorithm based on a penalty function formulation to impose the incompressibility constraint and a Petrov–Galerkin stabilization, using bilinear quadrilateral elements in two dimensions and trilinear 'bricks' in three dimensions [50]. The details of the numerical models have been given in [51–53] and will not be repeated here.

The most important deficiency of these models is their lack of efficiency. Except for the numerical implementations in [34,35] that used an explicit fractional step method to solve the momentum equations, all other models pursue implicit solutions of the momentum equation. This has severely limited the capability of the methods to model realistic casting dimensions, because of the high resolution required in the mushy zone to capture the relevant instabilities. Simulations involving dimensions of several centimeters O(10 cm) are possible in two dimensions, while in three dimensions the few published simulations are restricted to spatial dimensions on the order of 0.5–3.0 cm [54–56].

The most CPU-intensive and memory demanding part of the calculations is the solution of the momentum equation. It is well known that the fractional step method provides the most efficient way to solve the flow problem; however, in [34,35], and other references by the same authors [57,58], relatively coarse meshes were used in the discretization, and they have not reported applications that require very large meshes. A more recent implementation of the fractional step method has been reported in [59], where three-dimensional finite element simulations utilizing meshes of tri-linear elements of up to up to 200 000 nodes are presented. The author, however, encountered significant difficulties in the application of the method, which are discussed in [59].
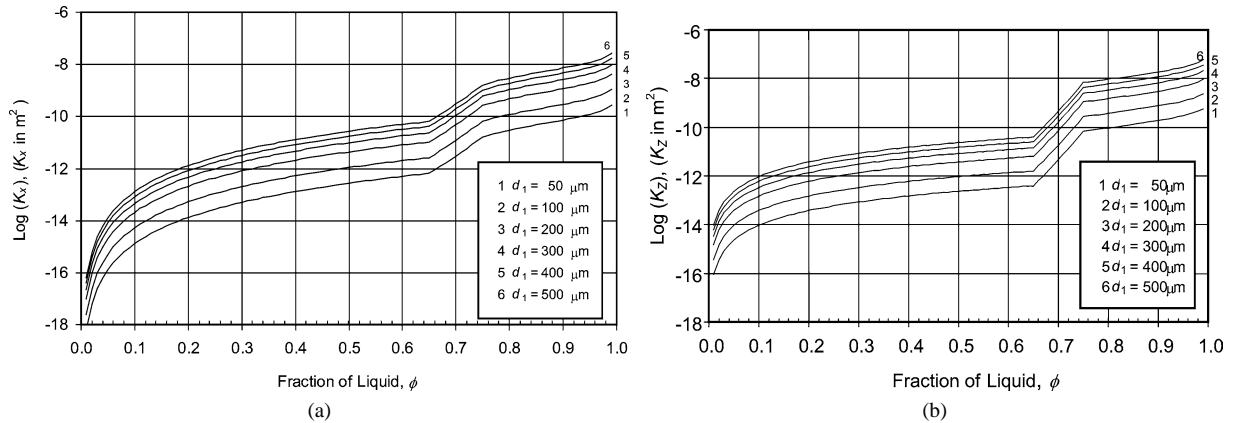
Fig. 2. Permeability (a) perpendicular and (b) parallel to the direction of solidification as a function of volume fraction of liquid, ϕ and primary dendrite arm spacing, d_1.

Fig. 2. Variation de la perméabilité (a) perpendiculaire et (b) parallèle à la direction de solidification en fonction de la fraction volumique du liquide, ϕ, et de l'espacement primaire entre dendrites, d_1.

A second source of difficulty in solidification simulations involving a mushy zone stems from the permeability tensor. The permeability varies from zero in the all-solid region to infinity in the all-liquid layer, which poses considerable numerical difficulty especially deep in the mushy zone. Also a problem has been a lack of knowledge of the precise form of the permeability. Some authors have been satisfied with the use of an isotropic permeability given by the Kozeny–Carman approximation [60]. But the Kozeny–Carman equation is valid for only about 0 to 50% solid; furthermore, the permeability is anisotropic and could be a source of discrepancies between numerical simulations. In this work, the permeability used in the principal directions is given by

$$K_x = K_y = \begin{cases} 1.09 \times 10^{-3} \phi^{3.32} d_1^2, & \phi \leqslant 0.65 \\ 4.04 \times 10^{-6} \left[\dfrac{\phi}{1-\phi} \right]^{6.7336} d_1^2, & 0.65 < \phi \leqslant 0.75 \\ \left(-6.49 \times 10^{-2} + 5.43 \times 10^{-2} \left[\dfrac{\phi}{1-\phi} \right]^{0.25} \right) d_1^2, & 0.75 < \phi \leqslant 1.0 \end{cases} \tag{14}$$

$$K_z = \begin{cases} 3.75 \times 10^{-4} \phi^2 d_1^2, & \phi \leqslant 0.65 \\ 2.05 \times 10^{-7} \left[\dfrac{\phi}{1-\phi} \right]^{10.739} d_1^2, & 0.65 < \phi \leqslant 0.75 \\ 0.074 \left[\log(1-\phi)^{-1} - 1.49 + 2(1-\phi) - 0.5(1-\phi)^2 \right] d_1^2, & 0.75 < \phi \leqslant 1.0 \end{cases} \tag{15}$$

Eq. (15) gives the permeability (m^2) in the direction parallel to dendrite growth, and Eq. (14) is for flow in the transverse direction to dendrite growth; d_1 is the primary dendrite arm spacing (m). When $\phi \leqslant 0.65$, the permeability above was obtained by means of a regression analysis of the available empirical data [61]. There are no empirical data when $\phi > 0.65$; therefore, in this range the permeability was obtained numerically as explained in [62–64]. A summary of the procedure used to merge the empirical and numerical data is given in [65].

The components of the permeability as a function of ϕ are shown in Fig. 2 for various values of d_1. The permeability in Fig. 2 exhibits a behavior between $0.65 \leqslant \phi \leqslant 0.75$ that may be puzzling to the reader. Examination of the empirical and numerical data shown in Fig. 6 of [62] and in Fig. 10 of [63] indicates that for values below $\phi = 0.65$ the data show a very different trend than for those above $\phi = 0.75$, requiring a different fit in each region. In order to best represent the existing data a separate region was introduced between $0.65 \leqslant \phi \leqslant 0.75$ as given in Eqs. (14) and (15). Numerical simulations in [62–64] were carried out to obtain the permeability for fractions of

liquid of up to 0.99, between 0.99 and 1.0 the formulas extrapolate the data and in some applications it would be desirable to extend the data up to $\phi = 0.999$, especially when looking at the nucleation of channel sites at the top of the mushy zone. Also more study is needed on the ability of the numerical methods to compute at very low values of ϕ, where the permeability becomes extremely small. If the dendritic growth is not aligned with the principal axis, then the permeability has to be locally transformed. A strategy to compute the Darcy term has been given in [66] for the two-dimensional case. Finally, an analysis of the momentum equations that takes into account the evolving nature of the heterogeneities in the permeability is found in [67] that shows the influence of the geometry of the dendritic structures on the evaluation of the permeability components.

There remain two more aspects of the model that require special attention; these are the way in which remelting is modeled and the solidification of the eutectic liquid. Remelting is an essential mechanism in the formation of channels and ultimately of freckles, and occurs when $\partial \phi / \partial t > 0$ at some location in the mushy zone, without necessarily achieving $\phi = 1$. For remelting to take place either the temperature or the solute concentration in the interdendritic liquid must increase at this location (when $k < 1$). Temperature is very unlikely to increase, due to the fact that heat is being extracted and due to the low value of the Prandtl number in alloys that make heat diffusion dominant over convection. On the other hand, mass diffusivities are relatively low, so when the concentration increases by advection of solute-rich liquid to a site where a channel is nucleating, remelting occurs. This can be seen by referring to Fig. 1. Within the mushy zone, the solutal concentration of the interdendritic liquid follows the liquidus line. At some point if the solute concentration increases while keeping the temperature constant, then the point (T, C_ℓ) will move to the right of the liquidus line into the liquid region of the phase diagram, indicating that remelting must take place. Some solidification models assume that solute diffuses infinitely fast in the solid; in this case, when remelting occurs it can be assumed that the composition of the remelting solid is the current solid composition and no special care needs to be taken. However, if it is assumed that there is no diffusion in the solid, then the composition of the solid depends on the solidification history, which must be saved in order to correctly account for microsegregation in the remelting solid [33]. This results in a large demand on computer-storage, because the sites of channels are not known a priori and this forces the modeler to develop strategies to retain the solidification history at every computational node.

In the model under consideration the solidification process is driven by the solute concentration and the temperature, which are tied up by Eq. (13) in the mushy zone. When the interdendritic liquid reaches the eutectic temperature, however, it solidifies at constant temperature when no undercooling of the eutectic reaction is assumed. This aspect of the models has been rarely discussed in the literature, and in some cases it has been handled incorrectly. In formulations based on enthalpy, such as in [28,32,40], the formulation is still valid at eutectic temperature; however, in models based on temperature the formulation must be modified when eutectic temperature is reached. This makes enthalpy formulations more convenient; however, they still require an algebraic transformations relating enthalpy to temperature. In models based on temperature the burden of dealing with solidification at the eutectic temperature is transferred to the numerical model. In [33,51], when a node reaches eutectic temperature, solidification is forced to continue at a constant temperature. The energy equation is modified by setting the time derivative to zero and used to calculate the volume fraction of liquid. The convective terms can also be neglected, and Eq. (10) becomes

$$\frac{\partial \phi}{\partial t} = \frac{1}{\rho_s[(c_{p_s} - c_{p_\ell})(T_H - T) + L]} \nabla \cdot \kappa \nabla T \tag{16}$$

Eq. (14) is solved at nodes where $T = T_E$ and Eq. (10) at all other nodes. This strategy has proven to be adequate when solidification is effected under the influence of gravity, and solidification contraction is not important ($\beta = 0$). Under microgravity, when convection is due solely to solidification contraction, the strategy does not model the velocity field properly, because physically the eutectic isotherm advances continuously through the domain and does not stay at the eutectic temperature over a finite period of time at the nodes. This model of eutectic solidification produces oscillations in the induced velocity that can be more than an order of magnitude greater than the correct velocity. Because these velocities are very small as compared with those induced by thermosolutal

convection, this is not a problem when solidification takes place under terrestrial gravity conditions, but they are unacceptable in microgravity. A method that allows the eutectic isotherm to move continuously through the elements has recently been developed and reported in [43]; in there it is also shown that when solidification contraction is the only form of convection, inverse segregation at a cooled surface can be correctly modeled (see, e.g., [16,68]), which other existing models had not been able to accomplish.

4. Examples of applications

A two-dimensional calculation simulating the upward solidification of a Pb-23.4 wt% Sn alloy is now discussed. The initial temperature gradient is 7700 K/m, and the bottom of the alloy is cooled at the rate of 0.05 K/s, so as

Table 1
Physical properties for Pb–Sn alloys

Tableau 1
Propriétés physiques des alliages Pb–Sn

Average thermal diffusivity	1.1×10^{-5}	$\text{m}^2\,\text{s}^{-1}$
Latent heat of fusion	37.6	$\text{kJ}\,\text{kg}^{-1}$
Average specific heat	0.176	$\text{kJ}\,\text{kg}^{-1}\,\text{K}^{-1}$
Thermal expansion coefficient	1.16×10^{-4}	K^{-1}
Solutal expansion coefficient	4.9×10^{-3}	$(\text{wt\%})^{-1}$
Solutal diffusivity	3.0×10^{-9}	$\text{m}^2\,\text{s}^{-1}$
Kinematic viscosity	2.47×10^{-7}	$\text{m}^2\,\text{s}^{-1}$
Equilibrium partition ratio	0.31	
Average density	9250.0	$\text{kg}\,\text{m}^{-3}$
Melting temperature of lead	600.0	K
Eutectic temperature	456.0	K
Eutectic concentration	61.9	wt% Sn
Acceleration of gravity	9.8	$\text{m}\,\text{s}^{-2}$
Interdendritic arm spacing	1.85×10^{-4}	m
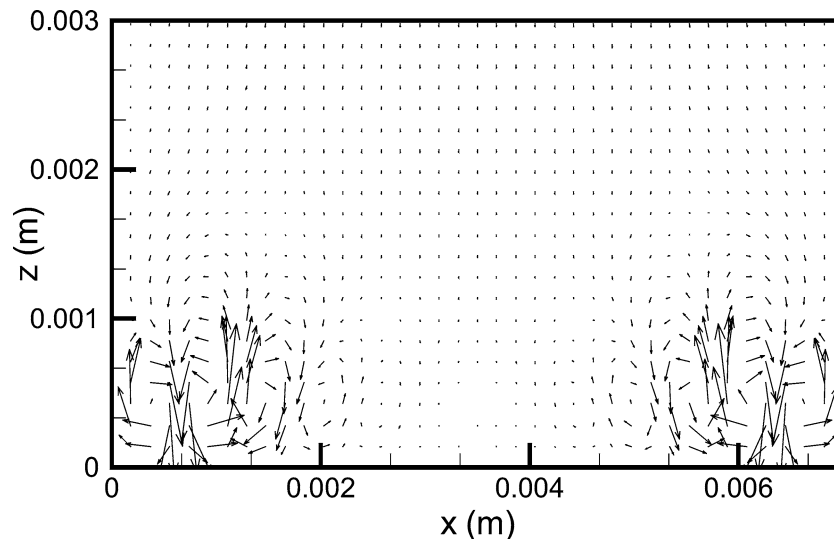
Fig. 3. Flow field at the bottom of the container in solidification of Pb-23.4 wt% Sn after 50 s of simulation.
Fig. 3. Champ des vitesses en bas du creuset après 50 secondes de simulation de la solidification de l'alliage Pb-23,4 % en poids Sn.

to produce an approximate solidification velocity of 6 μm/s. For simplicity the physical properties in the solid and in the liquid are assumed to be the same; these are listed in Table 1. This case was chosen because it was deemed unstable in [2]; it exhibits strong freckling and large variations in the convection patterns during the solidification. The calculation was performed on a uniform mesh of 38 by 190 bilinear elements. Initially the bottom of the container is at 545.5 K, slightly above the melting temperature of the alloy, and the uniform vertical temperature gradient is imposed everywhere else. No slip conditions are imposed along all surfaces in the all-liquid region; in the mushy zone slip is allowed along the vertical surfaces. The latter are assumed to be adiabatic; on the top the initial temperature gradient is maintained. Solidification is effected by lowering the temperature at the bottom at the specified linear rate in time.

After 50 s, we can observe the first convection cells beginning to form at the bottom (Fig. 3), where it can also be observed that the mushy zone has developed up to about 0.2 mm and the solidification front is still flat. The convection is very weak at this point; the maximum magnitude of the velocity is 6.3×10^{-3} mm/s. This stage of the process corresponds to what is usually called finger convection; because it comprises many small cells confined very close to the advancing solidification front, and corresponds to the boundary-layer mode of instability. At 100 s
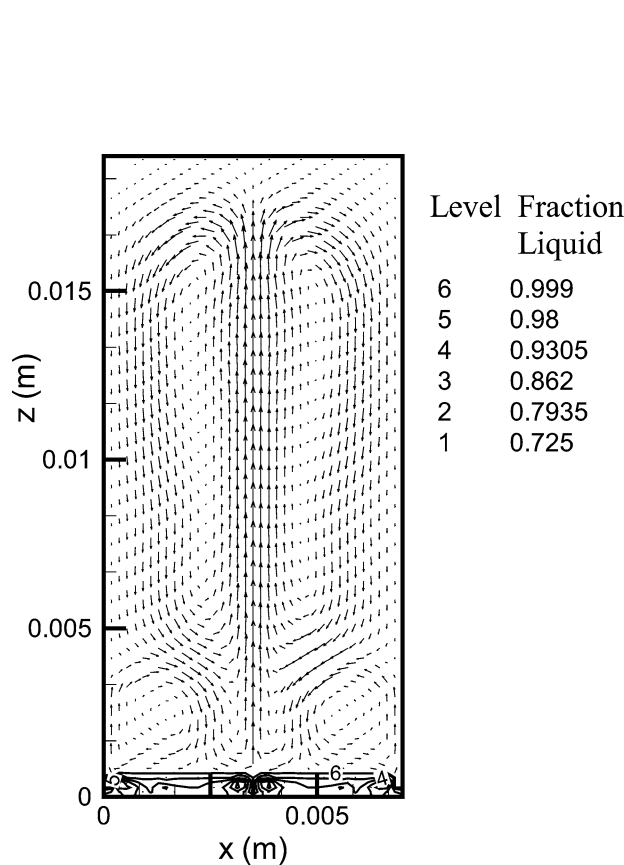
Fig. 4. Flow field and volume fraction of liquid in solidifying Pb-23.4 wt% Sn after 100 s of simulation.

Fig. 4. Champ des vitesses et fraction volumique du liquide après une simulation de 100 secondes de la solidification de l'alliage Pb-23,4 % en poids Sn.
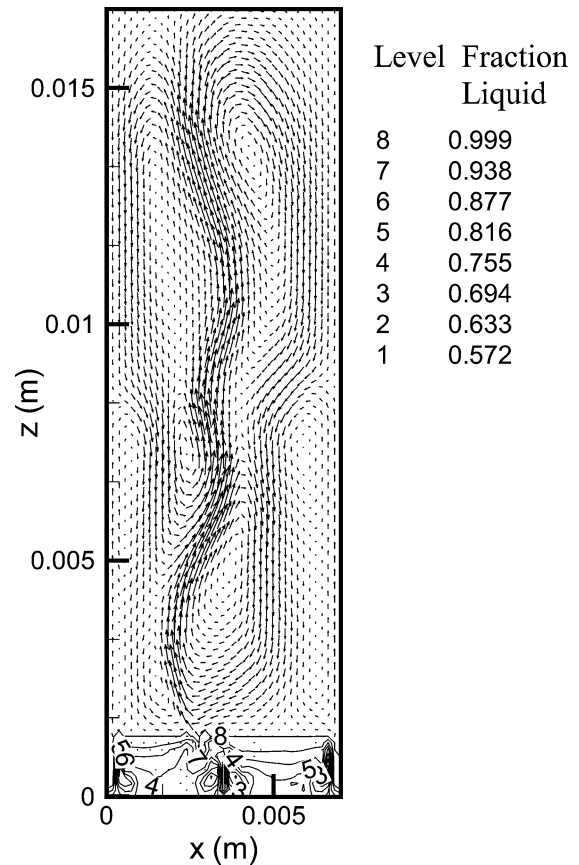
Fig. 5. Flow field and volume fraction of liquid in solidifying Pb-23.4 wt% Sn after 200 s of simulation.

Fig. 5. Champ des vitesses et fraction volumique du liquide après une simulation de 200 secondes de la solidification de l'alliage Pb-23,4 % en poids Sn.

Level	Fraction Liquid
6	0.999
5	0.9136
4	0.8282
3	0.7428
2	0.6574
1	0.572

Level	Fraction Liquid
10	0.999
9	0.889222
8	0.779444
7	0.669667
6	0.559889
5	0.450111
4	0.340333
3	0.230556
2	0.120778
1	0.011
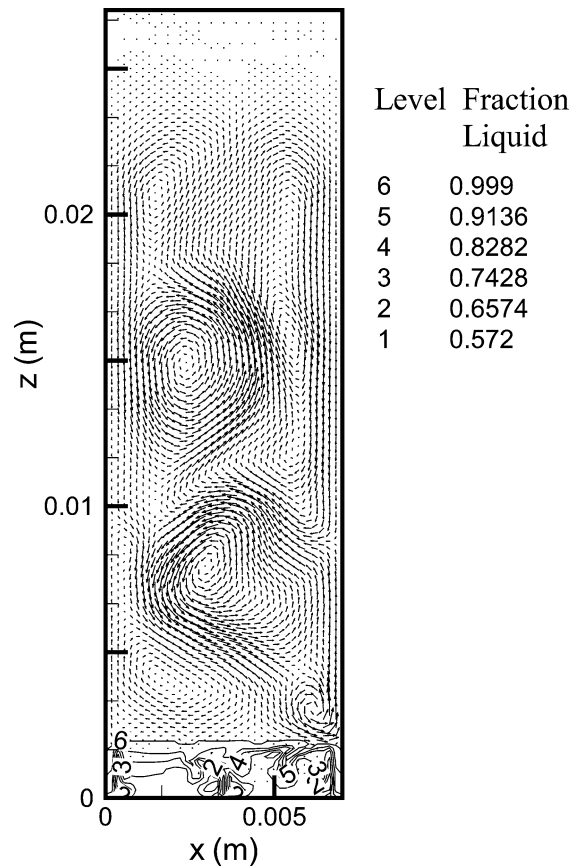
Fig. 6. Flow field and volume fraction of liquid in solidifying Pb-23.4 wt% Sn after 300 s of simulation.

Fig. 6. Champ des vitesses et fraction volumique du liquide après une simulation de 300 secondes de la solidification de l'alliage Pb-23,4 % en poids Sn.
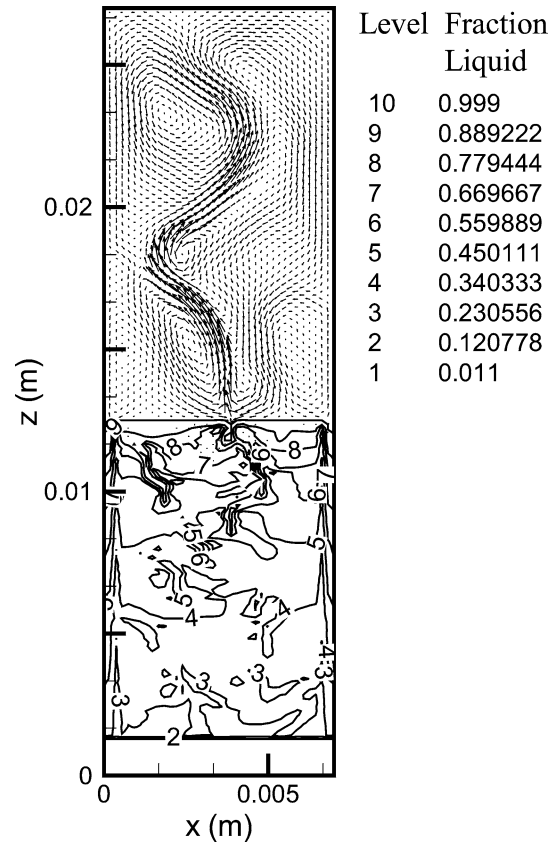
Fig. 7. Flow field and volume fraction of liquid in solidifying Pb-23.4 wt% Sn after 2000 s of simulation.

Fig. 7. Champ des vitesses et fraction volumique du liquide après une simulation de 2000 secondes de la solidification de l'alliage Pb-23,4 % en poids Sn.

the mode of convection is undergoing a transition towards a state similar to what is referred to as the mushy-layer mode of instability in [69], giving rise to a plume at the center of the container and two weaker plumes along the side walls, as shown in Fig. 4. The large cells induced by the center plume reach to about 1.8 cm high, and the maximum velocity reaches 2.1 mm/s. The mushy zone has advanced to 0.8 mm from the bottom. Fig. 5 shows the system after 200 s, the flow has completed its transition, a strong plume is observed close to the center, and the appearance of "volcanoes" is evident at the top of the mushy zone. Convection still has not reached the top of the overlying liquid and the system of organized cells observed previously in Fig. 4 has become unstable. At this point the convection cells begin to meander, grow and weaken and appear and disappear. This is the source of a great deal of localized segregation as will be shown below. To illustrate this almost chaotic behavior compare Fig. 5 with Fig. 6 at 300 s, where a very different convection pattern is observed. The maximum velocity at 200 s is 1.9 mm/s, and at 300 s it is 1.4 mm/s.

Next, Fig. 7 shows the simulation at 2000 s; the mushy zone is now fully developed, and the bottom 1.25 mm are fully solidified. The depth of the mushy zone is approximately 1.13 cm, which compares very well with the value of 1.16 cm that can be estimated from the temperature gradient and the phase diagram. The maximum
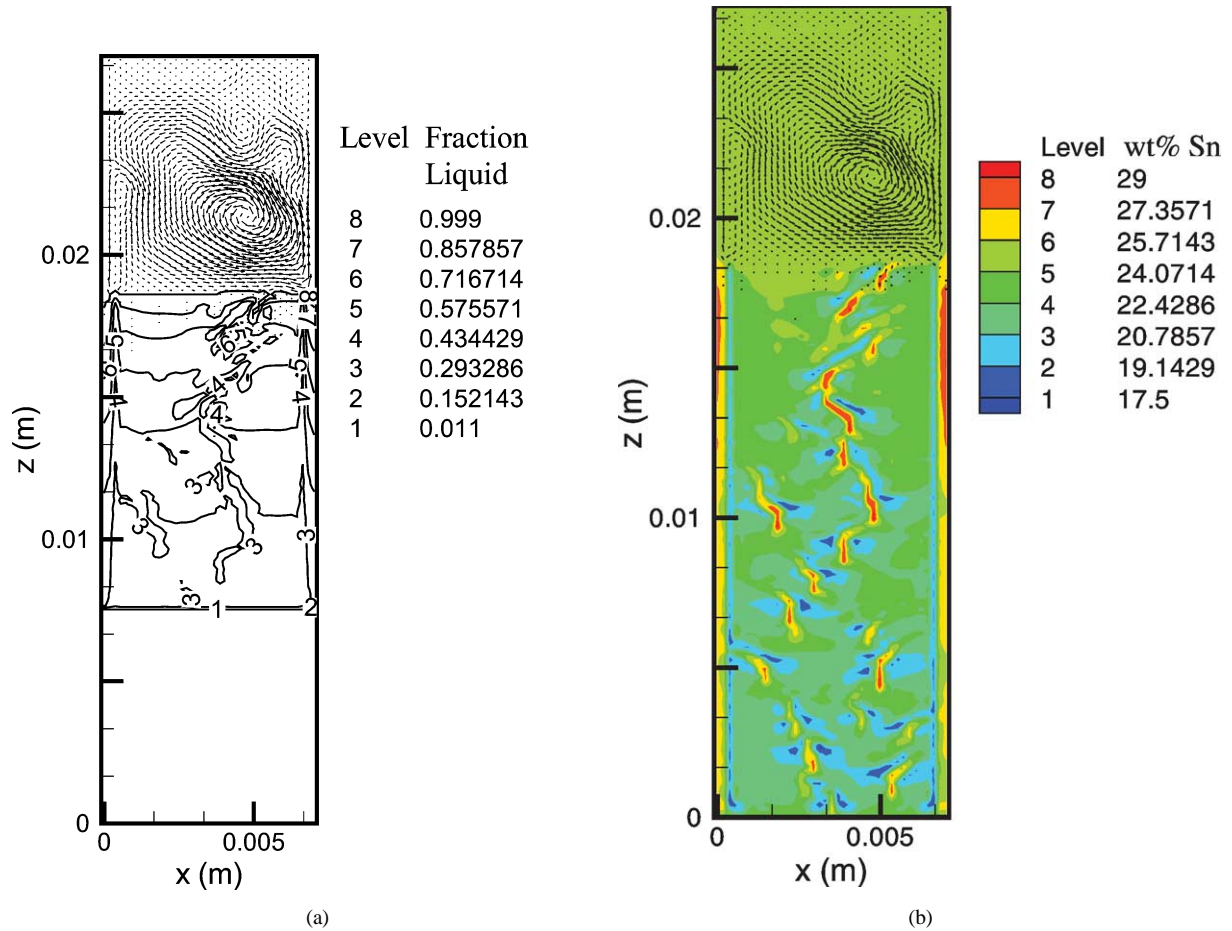
Fig. 8. Solidifying Pb-23.4 wt% Sn after 2000 s of simulation: (a) flow field and volume fraction of liquid; (b) flow field and total solute concentration.

Fig. 8. Alliage Pb-23,4 % en poids Sn après 2000 secondes de simulation de la solidification : (a) champ des vitesses et fraction volumique du liquide ; (b) champ des vitesses et concentration totale de soluté.

velocity at this point in time is 1.9 mm/s. The steps followed in Figs. 3–7 can be compared qualitatively with the experimental results shown in Fig. 3 of [70]; while keeping in mind that the experiments were performed in a solution of NH_4Cl–H_2O in which the fraction of liquid remains high throughout the mushy zone, that lead to very stable channels in the interior of the container. The last results shown in this calculation are at 3000 s of solidification and are shown in Figs. 8(a) and 8(b). In Fig. 8(a) the mushy zone has advanced at a speed of about 6.3 µm/s. The bottom 7.6 mm are fully solidified, and convection has weakened significantly due to the small amount of liquid remaining; the maximum velocity is only 0.6 mm/s. The final composition in the fully solidified region can be observed in Fig. 8(b); channels are obvious next to the vertical sides of the domain. For systems like this one, in which convection is strong and variable, long freckles do not develop in the interior due to the continuous changes in the convection pattern in the overlying liquid; rather they tend to change direction with the convection and disappear. However, the physical mechanisms still act in a way that is consistent with the analysis of [71], where it was assumed that fully developed channels have vertical sidewalls. Strong localized segregation
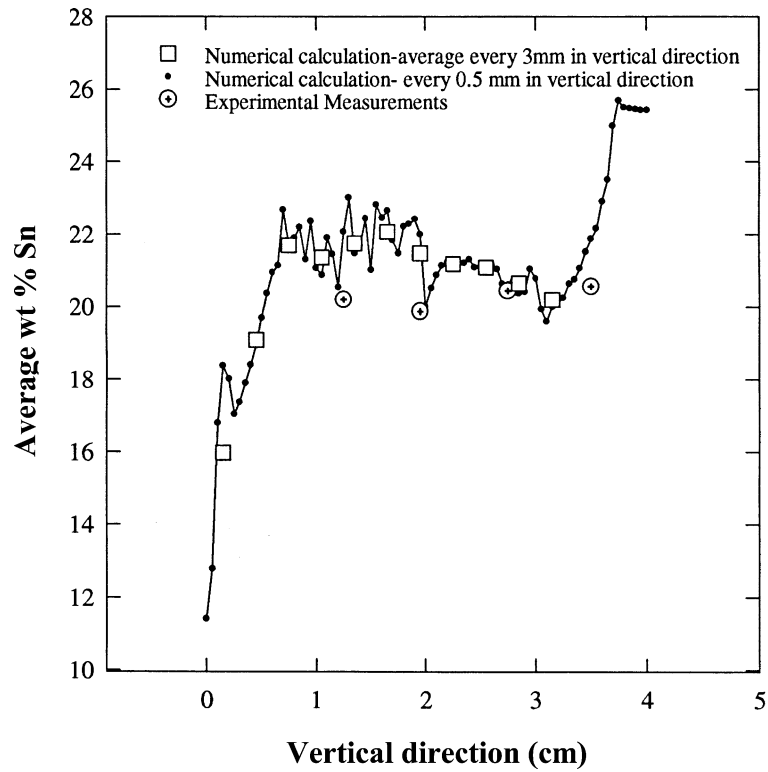
Fig. 9. Comparison of calculated and experimentally measured average concentrations in a Pb-23.2 wt% Sn alloy solidified vertically.

Fig. 9. Comparaison des concentrations moyennes calculées et mesurées expérimentalement pour l'alliage Pb-23,4 % en poids Sn solidifié verticalement.

can be observed in the interior along with the freckles along the vertical surfaces. The segregation in the freckles reaches 11.5 wt% Sn.

Validation of the two-dimensional results of simulations of solidification has been carried out by comparison with experimental results in Pb–Sn alloys solidified directionally and reported in [2,40,58]; very good agreement between experiments and simulations was found. In the case of vertical solidification a validation is presented in [72], where the experimental conditions reported in [73] were used. The experimental results were presented in the form of average concentrations across horizontal sections of a cylindrical ingot. These results together with those of a two-dimensional numerical simulation averaged every 3 and 5 mm in the vertical direction are shown in Fig. 9 and also show very good agreement, even though the details of macrosegregation cannot be compared. In [2], agreement between them was found on the basis of comparing whether freckles form in the experimental ingots and simulations.

The effect of variable density is best shown assuming that solidification takes place in the absence of gravity. A simulation using the same parameters as the one described above, except that the solid and liquid densities differ and the gravitational acceleration is set to zero, is shown next. The densities are $\rho_s = 9700$ kg/m^3 and are $\rho_l = 8900$ kg/m^3; the container is 7 mm wide and 40 mm tall. Fig. 10 shows the results after 3000 s of solidification. The flow is driven solely by solidification contraction; to maintain continuity, liquid is allowed to enter the container at the top at a uniform vertical velocity. In Fig. 10 it can be observed that the mushy zone is at approximately the same position as in the case of solidification under terrestrial gravity. Starting at the top, the flow develops into a Poiseuille flow in the all-liquid region, and it suffers a transition shortly before reaching the top of
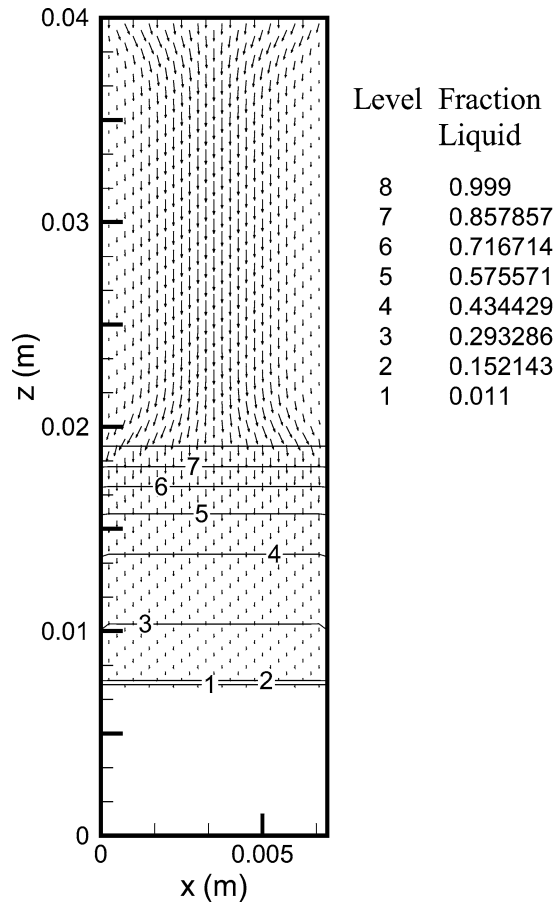
Fig. 10. Contraction induced flow under zero gravity, and volume fraction of liquid after 3000 s of solidification.

Fig. 10. Ecoulement induit par la contraction en apesanteur et fraction volumique du liquide après 3000 secondes de solidification.
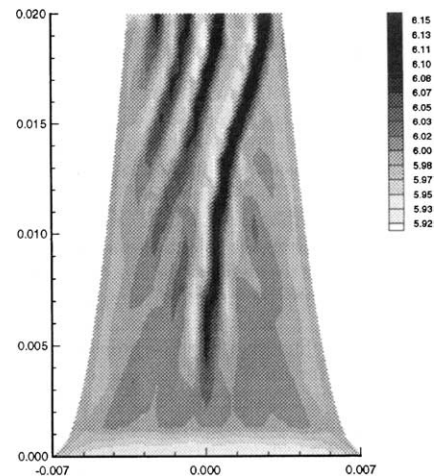
Fig. 11. Solidified Ni–Al–Ta–Cr alloy on a smoothly convergent container.

Fig. 11. Alliage Ni–Al–Ta–Cr solidifié dans un creuset à rétrécissement continu.

the mushy zone, where it turns into Darcy flow. The inflow at the top scales correctly with the volume contraction given by $\int_{\Omega} \beta(\partial\phi/\partial t)\,d\Omega$. In this case the velocity of the liquid feeding the contraction flow is 6.5×10^{-4} mm/s. As it penetrates the mushy zone, the liquid slows due to the decrease in liquid demand by the solidification volume. At the interface with the all-solid region, the velocity V_I of the liquid is related to the velocity V_E of the eutectic isotherm by $V_I = -\beta V_E$; in this calculation $V_I = 1.45 \times 10^{-4}$ mm/s. In [43] it was shown that V_I and the velocity of the liquid entering the top of the domain are approximated to within 1% of the expected steady-state velocities obtained from the temperature gradient and the cooling rate. In these simulations there is no evidence of segregation of the alloy, except at the bottom of the container, where inverse segregation occurs [16]. The inverse segregation is properly captured by the model and has been discussed in [43]. Calculations that show the liquid instabilities as the gravitational acceleration is increased and issues related to the calculation of the pressure in the mushy zone have been presented in [48,53].

Simulations of solidification of multicomponent alloys have been presented in [47,52,56,74–76]. In [47] and [52] the ternary Ni-base alloy Ni-5.8 wt% Al-15.2 wt% Ta alloy was used to calculate in a 7 mm by 20 mm rectangular domain. In this case, as Al is partitioned to the interdendritic liquid it has the effect of decreasing
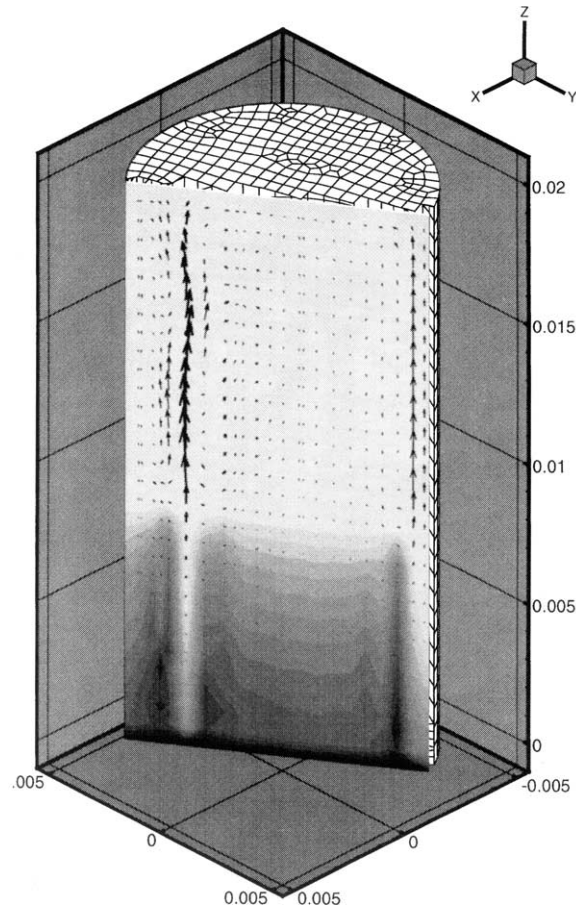
Fig. 12. Solidification of a three-dimensional Pb-10 wt% Sn alloy. Flow field and volume fraction of liquid after 10 minutes of simulation.

Fig. 12. Solidification tridimensionnelle d'un alliage Pb-10 % en poids Sn. Champ des vitesses et fraction volumique du liquide après 10 minutes de simulation.

the density of the liquid-alloy, but Ta increases the density of the liquid alloy. Simulations showed strong but very stable thermosolutal convection that led to well-defined freckles in the interior of the mushy zone as well as at the vertical surfaces of the alloy. Simulations for a quaternary alloy of Ni-6 wt% Al-6 wt% Ta-8 wt% Cr on variable geometries showed that narrow sections are more prone to develop freckling. The segregation of aluminum in one such calculation is shown in Fig. 11. The domain is 14 mm wide at the base, 20 mm tall and contracts symmetrically to 7 mm wide at the top. The temperature gradient and cooling rate are 5000 K/m and -0.28 K/s, respectively. Fig. 11 shows no evidence of freckling at the bottom of the container and strong channel segregation at the top.

One of the most serious difficulties encountered in the simulation of multicomponent alloys is the lack of reliable thermophysical data, [77]. Finally, in Fig. 12, a simulation of a three-dimensional solidification simulation of a binary Pb-10 wt% Sn alloy is shown [55]. The container is a cylinder of diameter 10 mm and 20 mm tall, under a thermal gradient of 1000 K/m and a cooling rate of 0.167 K/s. The cross section in Fig. 11 shows two freckles developing, one on the side wall and one in the interior, and plumes emanating from the channels. The results are after 10 minutes of solidification; five freckles develop with four of them next to the vertical surface and an interior one.

5. Conclusions

Mathematical models of solidification of multicomponent dendritic alloys at the mesoscale level have been discussed based on conservation equations that were derived using volume averaging and implemented with the finite element method. The need for sound mathematical models of solidification has been explained, and the effects of convection in the macrosegregation and the formation of freckles have been demonstrated for simulations in two and three dimensions. The learned reader will notice that almost no mention has been made of the extensive work in stability analysis and experiments related to this subject. This has been a conscious decision in an attempt to keep the presentation clear and focused on the numerical modeling aspects of the problems. Significant progress has been made in the subject area during the last twenty years; however, there still remain aspects that are in need of further study. Some of the remaining problems that have been identified are: the lack of efficiency of the existing numerical codes that prevent us from performing simulations in geometries with the dimensions of real castings; the numerical difficulties introduced by the low values of the permeability deep in the mushy zone; and the lack of thermophysical data for calculations in multicomponent alloys. Work in the first two areas continues to be pursued by the authors and colleagues, and the results will be reported in the future.

References

[1] G.J.S. Higginbotham, From research to cost-effective directional solidification and single-crystal production – an integrated approach, Mater. Sci. Tech. 2 (1986) 442–460.

[2] C. Frueh, D.R. Poirier, S.D. Felicelli, Predicting freckle-defects in directionally solidified Pb–Sn alloys, Mat. Sci. Engrg. A 328 (2002) 245–255.

[3] M. McLean, Directionally Solidified Materials for High Temperature Service, The Metals Society, London, 1983.

[4] T.C. Midea, D. Schmidt, Casting simulation software survey, Modern Casting 89 (1999) 47–51.

[5] M. Cruchaga, D. Celentano, Numerical analysis of thermally coupled flow problems with interfaces and phase-change effects, Int. J. Comp. Fluid Dyn. 16 (2002) 247–262.

[6] D. Juric, G. Tryggvason, A front-tracking method for dendritic solidification, J. Comput. Phys. 123 (1996) 127–148.

[7] H.S. Udaykumar, R. Mittal, W. Shyy, Computation of solid–liquid phase fronts in the sharp interface limit on fixed grids, J. Comput. Phys. 153 (1999) 535–574.

[8] P. Zhao, J.C. Heinrich, Front – tracking finite element method for dendritic solidification, J. Comput. Phys. 173 (2001) 765–796.

[9] A. Karma, W.J. Rappel, Quantitative phase-field modeling of dendritic growth in two and three dimensions, Phys. Rev. E 57 (1998) 4323–4349.

[10] L.H. Ungar, R.A. Brown, Cellular interface morphologies in directional solidification IV. The formation of deep cells, Phys. Rev. B 31 (1985) 5931–5940.

[11] J.A. Warren, W.J. Boettinger, Prediction of dendritic growth and microsegregation patterns in a binary alloy using the phase-field method, Acta Metall. Mater. 43 (1995) 689–703.

[12] P. Zhao, M. Vénere, J.C. Heinrich, D.R. Poirier, Modeling dendritic growth of a binary alloy, J. Comput. Phys. 188 (2003) 434–461.

[13] J.S. Kirkaldy, W.V. Youdelis, Contribution to the theory of inverse segregation, Trans. TMS-AIME 212 (1958) 833–840.

[14] M.C. Flemings, G.E. Nereo, Macrosegregation: Part I, Trans. Metall Soc. AIME 239 (1967) 1449–1461.

[15] M.C. Flemings, G.E. Nereo, Macrosegregation: Part II, Trans. Metall Soc. AIME 242 (1968) 41–49.

[16] M.C. Flemings, G.E. Nereo, Macrosegregation: Part III, Trans. Metall Soc. AIME 242 (1968) 50–55.

[17] R. Mehrabian, M. Keane, M.C. Flemings, Interdendritic fluid flow and macrosegregation: Influence of gravity, Metall Trans. 1 (1970) 1209–1220.

[18] R. Mehrabian, M. Keane, M.C. Flemings, Experiments on macrosegregation and freckle formation, Metall. Trans. 1 (1970) 3238–3241.

[19] S. Kou, D.R. Poirier, M.C. Flemings, Macrosegregation in ESR ingots, Electric Furnace Proc. ISS-IAME 35 (1977) 221–228.

[20] S. Kou, D.R. Poirier, M.C. Flemings, Macrosegregation in rotated remelted ingots, Metall. Trans. B 9 (1978) 711–719.

[21] S.D. Ridder, F.C. Reyes, S. Chakravorty, R. Mehrabian, J.D. Nauman, J.H. Chen, H.J. Klein, Steady-state segregation and heat flow in ESR, Metall. Trans. B 9 (1978) 415–425.

[22] T. Fujii, D.R. Poirier, M.C. Flemings, Macrosegregation in a multicomponent low alloy steel, Metall. Trans. B 10 (1979) 331–339.

[23] D. Petrakis, M.C. Flemings, D.R. Poirier, Some effects of forced convection on macrosegregation, in: H.D. Brody, D. Apelian (Eds.), Modeling of Castings and Welding Processes, TMS-AIME, Warrendale, PA, 1981.

[24] C.D.R. Poirier, Convection of interdendritic liquid in unidirectionally solidified alloys, in: Proceedings of the U.S.–Japan Cooperative Science Program Seminar on Solidification Processing, Dedham, MA, 1983.

[25] S.D. Ridder, S. Kou, R. Mehrabian, Effect of fluid flow on macrosegregation in axi-symmetric ingots, Metall. Trans. B 12 (1981) 435–447.

[26] A.L. Maples, D.R. Poirier, Convection in the two-phase zone of solidifying alloys, Metall. Trans. B 15 (1984) 163–172.

[27] D.R. Poirier, M.C. Flemings, R. Mehrabian, V. Weiss, Modeling macrosegregation in electroslag remelted ingots, in: J.J. Burke, R. Mehrabian, V. Weiss (Eds.), Advances in Metal Processing, Plenum, New York, 1981.

[28] W.D. Bennon, F.P. Incropera, A continuum model for momentum, heat and species transport in binary solid–liquid phase change systems-I. Model formulation, Int. J. Heat Mass Transfer 30 (1987) 2161–2170.

[29] S. Ganesan, D.R. Poirier, Conservation of mass and momentum for the flow of interdendritic liquid during solidification, Metall. Trans. B 21 (1990) 173–181.

[30] D.R. Poirier, P.J. Nandapurkar, S. Ganesan, The energy and solute conservation equations for dendritic solidification, Metall. Trans. B 22 (1991) 889–900.

[31] C. Beckermann, R. Viskanta, Mathematical modeling of transport phenomena during solidification, Appl. Mech. Rev. 46 (1993) 1–27.

[32] W.D. Bennon, F.P. Incropera, A continuum model for momentum, heat and species transport in binary solid–liquid phase change systems-II; applications to solidification in a rectangular cavity, Int. J. Heat Mass Transfer 30 (1987) 2171–2187.

[33] S.D. Felicelli, J.C. Heinrich, D.R. Poirier, Simulation of freckles during vertical solidification of a binary alloy, Metall. Trans. B 22 (1991) 847–859.

[34] G. Amberg, Computation of macrosegregation in an iron-carbon cast, Int. J. Heat Mass Transfer 34 (1991) 217–227.

[35] D. Xu, Q. Li, Numerical method for solution of strongly coupled binary alloy solidification problems, Numer. Heat Transfer A 20 (1991) 181–201.

[36] K.C. Chiang, H.L. Tsai, Shrinkage induced fluid flow and domain change in two-dimensional alloy solidification, Int. J. Heat Mass Transfer 35 (1992) 1763–1770.

[37] M.C. Schneider, C. Beckermann, A numerical study of the combined effects of microsegregation, mushy zone permeability and flow, caused by volume contraction and thermosolutal convection, on macrosegregation and eutectic formation in binary alloy solidification, Int. J. Heat Mass Transfer 38 (1995) 3455–3473.

[38] C.R. Swaminathan, V.R. Voller, Towards a general numerical scheme for solidification systems, Int. J. Heat Mass Transfer 40 (1997) 2859–2868.

[39] G.F. Naterer, Simultaneous pressure-velocity coupling in the two-phase zone for solidification shrinkage in an open casting, Model. Simul. Mater. Sci. Engrg. 5 (1997) 595–613.

[40] N. Ahmad, H. Combeau, J.-L. Desbiolles, T. Jalanti, G. Lesoult, J. Rappaz, M. Rappaz, C. Stomp, Numerical simulation of macrosegregation: a comparison between finite volume method and finite element method predictions and a confrontation with experiments, Metall. Mater. Trans. A 29 (1998) 617–630.

[41] V. Voller, C.M. Swaminathan, B.G. Thomas, Fixed grid techniques for phase change problems: a review, Int. J. Numer. Methods Engrg. 30 (1990) 875–898.

[42] C. Beckermann, Modeling of macrosegregation: applications and future needs, Int. Mater. Rev. 47 (2002) 243–261.

[43] J.C. Heinrich, D.R. Poirier, Effect of volume change during directional solidification of binary alloys, Model. Simul. Mater. Sci. Engrg. (2004), in press.

[44] D.A. Nield, The boundary correction for the Rayleigh–Darcy problem: limitations of the Brinkman equation, J. Fluid Mech. 128 (1983) 37–46.

[45] D.A. Nield, D.D. Joseph, Effect of quadratic drag on convection in a saturated porous medium, Phys. Fluids 28 (1985) 995–997.

[46] C. Beckerman, R. Viskanta, Double-diffusive convection during dendritic solidification of a binary mixture, Phys.-Chem. Hydrodyn. 10 (1988) 195–213.

[47] S.D. Felicelli, J.C. Heinrich, D.R. Poirier, Finite element analysis of directional solidification of multicomponent alloys, Int. J. Numer. Methods Fluids 27 (1998) 207–227.

[48] J.C. Heinrich, E. McBride, Calculation of pressure in a mushy zone, Int. J. Numer. Methods Engrg. 47 (2000) 735–747.

[49] G. Amberg, Parameter ranges in binary solidification from vertical boundaries, Int. J. Heat Mass Transfer 40 (1997) 2565–2578.

[50] J.C. Heinrich, D.W. Pepper, Intermediate Finite Element Method; Fluid Flow and Heat Transfer Applications, Taylor & Francis, Philadelphia, 1999.

[51] S.D. Felicelli, J.C. Heinrich, D.R. Poirier, Numerical model for dendritic solidification of binary alloys, Numer. Heat Transfer B 23 (1993) 461–481.

[52] S.D. Felicelli, J.C. Heinrich, D.R. Poirier, Finite element analysis of directional solidification of multicomponent alloys, Int. J. Numer. Methods Fluids 27 (1998) 207–227.

[53] E. McBride, J.C. Heinrich, D.R. Poirier, Numerical simulation of incompressible flow driven by density variations during phase change, Int. J. Numer. Methods Fluids 31 (1999) 787–800.

[54] D.G. Nielson, F.P. Incropera, Three-dimensional considerations of unidirectional solidification in a binary liquid, Numer. Heat Transfer 23 (1993) 1–20.

[55] S.D. Felicelli, J.C. Heinrich, D.R. Poirier, Three-dimensional simulations of freckles in binary alloys, J. Crystal Growth 191 (1997) 879–888.

[56] S.D. Felicelli, D.R. Poirier, J.C. Heinrich, Modeling freckle formation in three dimensions during solidification of multicomponent alloys, Metall. Mater. Trans. B 29 (1998) 847–855.

[57] D. Xu, Q. Li, Gravity- and solidification-shrinkage-induced liquid flow in a horizontally solidified alloy ingot, Numer. Heat Transfer A 20 (1991) 203–221.

[58] H. Shahani, G. Amberg, H. Fredriksson, On the formation of macrosegregations in unidirectionally solidified Sn–Pb and Pb–Sn alloys, Metall. Trans. A 23 (1992) 2301–2311.

[59] D.G. Westra, Simulation of directional solidification in a binary alloy using the fractional step method, Ph.D. Dissertation, The University of Arizona, Tucson, 2003.

[60] A. Bejan, Convective heat transfer in porous media, in: S. Kakacs, R.K. Shah, W. Aung (Eds.), Handbook of Single Phase Convective Heat Transfer, Wiley, New York, 1987.

[61] D.R. Poirier, Permeability for flow of interdendritic liquid in columnar-dendritic alloys, Metall. Trans. B 18 (1987) 245–255.

[62] S. Ganesan, C.L. Chan, D.R. Poirier, Permeability of flow parallel to dendrite arms, Mater. Sci. Engrg. A 151 (1992) 97–105.

[63] M.S. Bhat, D.R. Poirier, J.C. Heinrich, Permeability for cross flow through columnar-dendritic alloys, Metall. Mater. Trans. B 26 (1995) 1049–1056.

[64] J.C. Heinrich, D.R. Poirier, D.F. Nagelhout, Mesh generation and flow calculations in highly contorted geometries, Comp. Methods Appl. Mech. Engrg. 133 (1996) 79–92.

[65] D.R. Poirier, J.C. Heinrich, Continuum model for predicting macrosegregation in dendritic alloys, Mater. Character. 32 (1994) 287–298.

[66] S.K. Sinha, T. Sundararajan, V.K. Garg, A variable property analysis of alloy solidification using the anisotropic porous medium approach, Int. J. Heat Mass Transfer 35 (1992) 2865–2877.

[67] B. Goyeau, T. Bennihaddadene, D. Gobin, M. Quintard, Averaged momentum equation for flow through a nonhomogeneous porous structure, Transp. Porous Media 28 (1997) 19–50.

[68] T. Motegi, A. Ohno, Inverse segregation in unidirectionally solidified Al–Cu alloy ingots, Trans. Japan Inst. Metals 25 (1984) 122–132.

[69] M.G. Worster, Instabilities of the liquid and mushy regions during solidification of alloys, J. Fluid Mech. 237 (1992) 649–669.

[70] C.F. Chen, F. Chen, Experimental study of directional solidification of aqueous ammonium chloride solutions, J. Fluid Mech. 227 (1991) 567–586.

[71] T.P. Schulze, M.G. Worster, A numerical investigation of steady convection in mushy layers during the directional solidification of binary alloys, J. Fluid Mech. 356 (1998) 199–220.

[72] H.W. Huang, J.C. Heinrich, D.R. Poirier, Simulation of directional solidification with steep thermal gradients, Model. Simul. Mater. Sci. Engrg. 4 (1996) 245–259.

[73] S.N. Tewari, R. Shah, Macrosegregation during steady-state arrayed growth of dendrites in directionally solidified Pb–Sn alloys, Metall. Trans. 23A (1992) 3383–3392.

[74] S.D. Felicelli, D.R. Poirier, J.C. Heinrich, Macrosegregation patterns in multicomponent Ni-base superalloys, J. Crystal Growth 177 (1996) 145–161.

[75] S.D. Felicelli, D.R. Poirier, A.F. Giamei, J.C. Heinrich, Simulation of the solidification of DS and SC superalloys, JOM 49 (1997) 21–25.

[76] M.C. Schneider, C. Beckermann, Formation of macrosegregation by multicomponent thermosolutal convection during solidification of steel, Metall. Mater. Trans. A 26 (1995) 2373–2388.

[77] S.D. Felicelli, P.K. Sung, D.R. Poirier, J.C. Heinrich, Transport properties and transport phenomena in casting nickel superalloys, Int. J. Thermophys. 19 (1998) 1657–1669.